EDGE ARTICLE

Check for updates

Inserting an "atomic trap" for directional dopant migration in core/multi-shell quantum dots†

Chun Chu,[a] Elan Hofman,[a] Chengpeng Gao,[a] Shuya Li,[a] Hanjie Lin,[a] Walker MacSwain, [ID] [a] John M. Franck,[a] Robert W. Meulenberg,[b] Arindam Chakraborty [ID] [a] and Weiwei Zheng [ID] *[a]

Diffusion of atoms or ions in solid crystalline lattice is crucial in many areas of solid-state technology. However, controlling ion diffusion and migration is challenging in nanoscale lattices. In this work, we intentionally insert a CdZnS alloyed interface layer, with small cationic size mismatch with Mn(II) dopant ions, as an "atomic trap" to facilitate directional (outward and inward) dopant migration inside core/multi-shell quantum dots (QDs) to reduce the strain from the larger cationic mismatch between dopants and host sites. Furthermore, it was found that the initial doping site/environment is critical for efficient dopant trapping and migration. Specifically, a larger Cd(II) substitutional site (92 pm) for the Mn(II) dopant (80 pm), with larger local lattice distortion, allows for efficient atomic trapping and dopant migration; while Mn(II) dopant ions can be very stable with no significant migration when occupying a smaller Zn(II) substitutional site (74 pm). Density functional theory calculations revealed a higher energy barrier for a Mn(II) dopant hopping from the smaller Zn substitutional tetrahedral (T_d) site as compared to a larger Cd substitutional T_d site. The controlled dopant migration by "atomic trapping" inside QDs provides a new way to fine tune the properties of doped nanomaterials.

Introduction

At the heart of materials chemistry is the ability to control materials' properties by tuning their chemical composition as reflected by the importance of alloying in metallurgy and doping in modern semiconductor technology.[1–3] Incorporating dopants inside a nanocrystal (NC) lattice is a fascinating method to modify and improve the optical, electrical, and magnetic properties of the NCs.[1–16] In addition to the chemical and physical properties of dopants, the dopant location and distribution can also have profound effects on the final properties of doped NCs because of the distance-dependent host-dopant coupling from the wavefunction overlap.[17,18] For example, in Mn doped metal chalcogenide NCs, the dopant photoluminescence (PL) peak around 600 nm arising from host-to-dopant energy transfer, is strongly influenced by the dopant locations inside the NCs as the energy transfer relies on the spatial overlap between the wavefunctions of the host exciton and dopants.[19–24] Therefore, the quantum yield (QY) of the Mn dopant PL peak is heavily dependent on the radial position and distribution of Mn ions inside the host

lattice.[4,17,25] Despite significant developments in the synthesis of doped NCs, dopant behavior after incorporation inside NCs is not well understood. Specifically, the control of dopant location and distribution inside NCs through directional dopant migration is still largely unexplored. Therefore, it is fundamentally important to understand the spatial distribution of dopants in NCs from a synthetic control aspect, and a necessity to understand how dopant manipulation affects the resulting properties.

Theoretically, facilitated dopant diffusion is possible, especially at relatively high temperatures, since the high thermal energy of dopant ions leads to higher hopping frequencies inside the host lattice.[26] In addition, dopant behaviors could be complicated in the host lattice, considering that thermal self-annealing effects can also induce outward movement of dopants in NCs. For example, dopant ejection could happen with extended thermal annealing of Mn doped QDs at high temperatures.[17,27] However, manipulating dopant location by migration or diffusion inside NC lattice after dopant incorporation is challenging due to the high activation energy of ion diffusion.[4,28] Additional challenges to control and study the dopant migration behavior pertains to limited analytical techniques available to the detection of the location and distribution of low concentration dopant ions (generally less than five percent) in NCs with high spatial and temporal resolution at the nanoscale.[20,29–31] Dopant ions inside NC lattice are extrinsic point defects, which could entail a significant local distortion of

[a]Department of Chemistry, Syracuse University, Syracuse, New York 13244, USA. E-mail: wzhen104@syr.edu

[b]Department of Physics and Astronomy and Frontier Institute for Research in Sensor Technologies, University of Maine, Orono, Maine 04469, USA
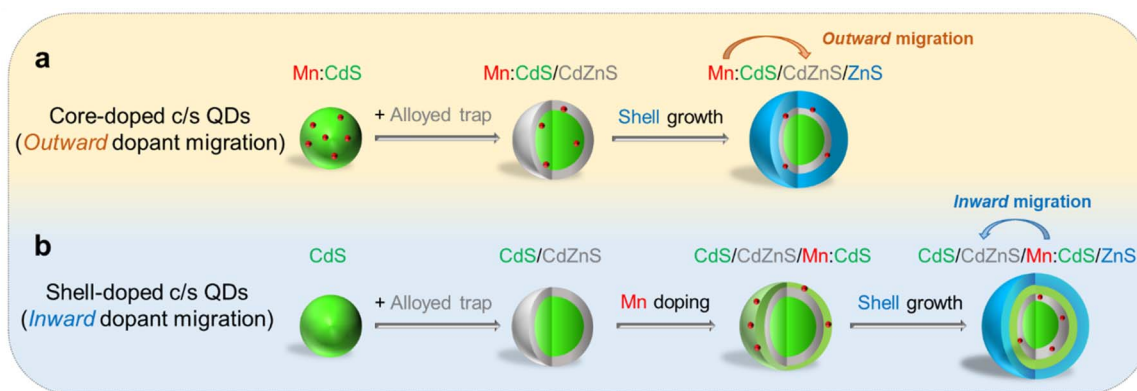
Scheme 1 Schematic of (a) core-doped and (b) shell-doped core/multi-shell QDs with directional (outward and inward) dopant migration by inserting an alloyed "trap" for Mn dopants.

the structure, especially with a large size mismatch with the host substitutional sites. Therefore, thermodynamically, the point defects can migrate to more ideal substitutional sites with smaller size mismatch.[26] However, whether the directional dopant migration can be controlled by intentionally inserted dopant "trap" layers with less size mismatch is unknown.

In this work, we systematically control the Mn dopant migration by inserting an alloyed interface with a smaller cationic size mismatch with Mn as an "atomic trap" within core/shell QDs for directional Mn dopant migration and therefore dopant location and distribution inside QDs. Both outward and inward Mn dopant migration behaviors were achieved by intentionally inserting a CdZnS alloyed layer into the core- and shell-doped core/shell QDs, respectively (Scheme 1). More importantly, it was found that the initial doping site is critical for efficient "atomic trapping" and dopant migration. Specifically, a larger initial Cd(II) substitutional site (92 pm) for Mn(II) dopants (80 pm) allows for efficient atomic trapping and dopant migration, while Mn(II) dopant ions can be very stable with no significant migration occurring when occupying a smaller Zn(II) substitutional site (74 pm). Theoretical simulations indicate a significantly high energy barrier for dopant hopping through a smaller substitutional tetrahedral (T_d) site. It is fundamentally important to understand the mechanism of directional dopant migration behavior within NC lattices, which plays a critical role in finely manipulating the properties of the doped NCs.

Results and discussion

In this work, Mn core-doped and shell-doped core/multi-shell QDs were designed and the directional migration behaviors of Mn ions in the QD lattice were studied under the influence of an inserted CdZnS layer as an "atomic trap" within core/multi-shell QDs. The outward dopant migration was studied by inserting alloyed interface layer (CdZnS) in Mn core-doped CdS/ZnS (i.e., Mn:CdS/CdZnS/ZnS) core/multi-shell QDs (Scheme 1a). While the inward dopant migration was investigated by inserting alloyed interface (CdZnS) in Mn shell-doped CdS/Mn:CdS/ZnS (i.e., CdS/CdZnS/Mn:CdS/ZnS) core/multi-shell QDs (Scheme 1b).

Controlled outward dopant migration in Mn core-doped core/multi-shell QDs

To facilitate the outward Mn dopant migration, Mn core-doped CdS QDs (i.e., Mn:CdS QDs) were synthesized first, followed by the growth of the CdZnS alloyed trap layer and up to 4 monolayers (MLs) ZnS shell (i.e., Mn:CdS/CdZnS/ZnS$_{(1-4 MLs)}$ core/multi-shell QDs) using a successive ionic layer adsorption and reaction (SILAR) method.[32] Mn:CdS/ZnS core/shell QDs without the alloyed shell were also synthesized in control experiments to verify the effect of the alloyed trap layer for dopant migration behavior (see Experimental section in the ESI†). The Mn:CdS QDs have an average size of 3.0 ± 0.3 nm from transmission electron microscopy (TEM) data. After additional 1 ML CdZnS and 4 ML ZnS shell growth, the size of the Mn:CdS/CdZnS/ZnS core/multi-shell QDs increased to 5.6 ± 0.3 nm (Fig. 1a–c and S1a†). On average, there is ∼0.5 nm increase in diameter for the addition of each shell ML for both Mn:CdS/CdZnS/ZnS and Mn:CdS/ZnS core/multi-shell QDs (Fig. S1†).

Powder X-ray diffraction (XRD) measurements reveal that the Mn:CdS core, Mn:CdS/ZnS$_{(1-5 MLs)}$ core/shell, and Mn:CdS/CdZnS$_{(1 ML)}$/ZnS$_{(1-4 MLs)}$ core/multi-shell QDs possess a cubic phase (Fig. 1d and S2a†). XRD patterns of the samples show a gradual peak shift from the cubic CdS to the cubic ZnS phase as the growth of the successive ZnS shell of the QDs (Fig. 1d and f). A dampening of the shift toward the ZnS cubic phase occurred when the CdZnS shells were grown on top of the core QDs (i.e., Mn:CdS/CdZnS$_{(1 ML)}$ QDs) due to the intermediate lattice parameters of the CdZnS, when compared to pure CdS or ZnS lattice based on the Vegard's law,[33] resulting in a smaller total shift (Fig. 1d and f). In addition, gradual narrowing of the full width at half maximum (FWHM) of the (111) diffraction peaks of the QDs during the successive shell growth (Fig. S2b†) is consistent with the larger QDs obtained after shell passivation.

Inductively coupled plasma-optical emission spectrometry (ICP-OES) measurements indicate the Mn doping concentration is 1.2% for Mn:CdS QDs, which represents ∼6 Mn(II) ions on average in a 3.0 nm Mn:CdS QD distributed statistically between the core and surface of the QD. The Mn(II) concentration decreases to 0.6% after the addition of the ZnS shell and
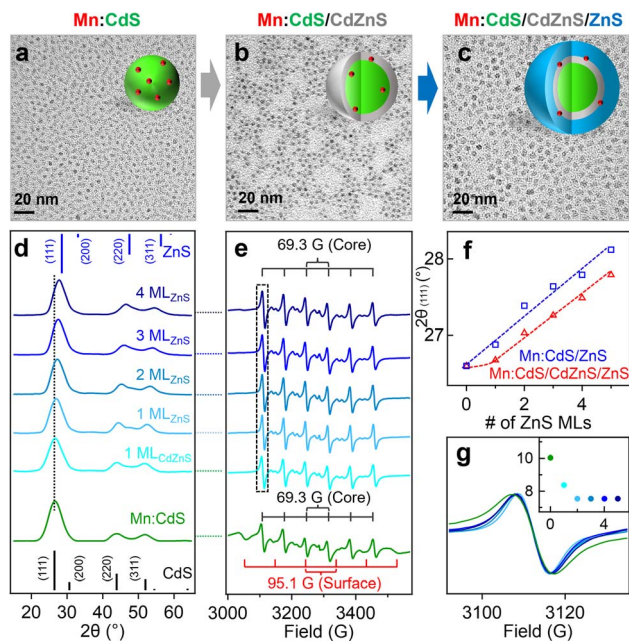
Fig. 1 (a–c) TEM images of Mn:CdS core, Mn:CdS/CdZnS core/shell, and Mn:CdS/CdZnS/ZnS$_{(4\ MLs)}$ core/multi-shell QDs. (d) XRD patterns and (e) X-band EPR spectra of Mn:CdS/CdZnS/ZnS$_{(1–4\ MLs)}$ core/multi-shell QDs. (f) The (111) diffraction peak position of the Mn:CdS/ZnS and Mn:CdS/CdZnS/ZnS core/multi-shell QDs as a function of the ZnS shell thickness. (g) The representative first sextet EPR hyperfine peak to display decreasing spectral linewidth with increasing shell thickness, inset shows the EPR hyperfine peak linewidth (in G) as a function of shell monolayers.

remains unchanged for the remainder of the CdS/ZnS core/shell QDs. The sudden drop could be attributed to the detachment of the loosely bound surface Mn(II), resulting in ~3 Mn(II) ions per QD.[21] Interestingly, the Mn:CdS/CdZnS/ZnS$_{(1–4\ MLs)}$ samples showed a slightly higher Mn(II) concentration of ~0.9%, which represents ~4 Mn(II) ions per core/multi-shell QD with an inserted CdZnS alloyed layer. The increased doping concentration for QDs with an added alloyed layer compared to Mn:CdS/ZnS core/shell QDs with pure, unalloyed ZnS shells can be understood by the CdZnS alloyed shell layer having a more accommodating lattice size for the Mn(II) to assimilate into.[34,35] It has been reported that the increased Mn(II) dopant concentration within the $Zn_xCd_{1−x}S$ alloyed host lattice compared with that in CdS and ZnS QD lattice is due to the reduced cationic size mismatch between the Mn ion and alloyed host lattice.[34,35]

Electron paramagnetic resonance (EPR) spectrum indicates that Mn ions substitute into both the core and surface lattice of Mn:CdS core QDs with hyperfine splitting constants (A) of 69.3 G and 95.1 G, respectively[20,34,36] (Fig. 1e). During shell passivation, the surface peaks disappeared and only one six-line pattern spectrum with A = 69.3 G remains which indicates successful surface passivation of the Mn:CdS QDs. Interestingly, the linewidth of the EPR hyperfine splitting decreases from 10.0 G for Mn:CdS, to 8.4 G for Mn:CdS/CdZnS, to 7.5 G for Mn:CdS/CdZnS/ZnS$_{(4\ MLs)}$ (Fig. 1g). Considering no significant change in the average Mn–Mn distance before and after dopant migration in the QDs (~1.6 nm, see ESI† for the calculation,

Tables S1, S2 and Scheme S1†), the narrower linewidth of the hyperfine splitting indicates less local strain on the Mn(II) dopant sites during shell passivation,[17,23] which could imply the change of dopant location to the cationic sites with less cationic size mismatch and strain in the core/multi-shell QDs. EPR spectra of the control Mn:CdS/ZnS$_{(1–5\ MLs)}$ samples show similar core and surface Mn signals with hyperfine splitting constants of 69.1 G and 96.3 G, respectively (Fig. S3a†). However, there is little change of the linewidth of the EPR hyperfine peak (from 10.0 G for the Mn:CdS core to 9.8 G for the Mn:CdS/ZnS core/ shell QDs) (Fig. S3b and c†), which indicates a less dramatic change in the Mn dopant bonding environment in Mn:CdS/ ZnS$_{(1–5\ MLs)}$ compared to the Mn:CdS/CdZnS/ZnS$_{(1–4\ MLs)}$ samples with an inserted alloyed layer.

Fig. 2a and b displays the absorption and PL spectra of the Mn:CdS core, Mn:CdS/ZnS$_{(1–5\ MLs)}$ core/shell, and Mn:CdS/ CdZnS$_{(1\ ML)}$/ZnS$_{(1–4\ MLs)}$ core/multi-shell QDs. The first exciton absorption peak for Mn:CdS core QDs at 405 nm experiences a slight redshift (2 nm) upon the addition of the first ZnS ML onto the core in Mn:CdS/ZnS core/shell QDs (Fig. 2a). The small spectrum shift could be attributed to the delocalization of the core electrons into the thin CdZnS alloyed interface that is formed between the CdS core and the ZnS shell lattice to reduce the surface strain for the epitaxial growth of the ZnS shell. A larger redshift of the first exciton absorption peak (20 nm shift, from 405 to 425 nm) is observed with the intentional growth of one CdZnS ML directly onto the Mn:CdS QDs for the Mn:CdS/ CdZnS/ZnS core/multi-shell QDs (Fig. 2b), which is consistent with the increased delocalization of the core electrons to the CdZnS alloyed shell with a smaller bandgap compared to that of ZnS lattice.[37]

A single broad emission peak centered at 575 nm (FWHM: 112 nm) is observed in the emission spectrum of the Mn:CdS core QDs (Fig. 2a and b), indicating the presence of surface trap-states overlapping with the Mn(II) emission. An immediate narrowing of the Mn(II) PL FWHM was observed after the first ML shell passivation in both CdS/ZnS and CdS/CdZnS/ZnS QDs (Fig. S4†), indicating the successful surface passivation to remove surface trap-states in the core/shell QDs. A new PL peak from the core CdS QDs at around 420 and 438 nm was observed after the growth of the first ZnS and CdZnS shell for Mn:CdS/ ZnS and Mn:CdS/CdZnS/ZnS QDs, respectively.

Interestingly, the PL ratio of the CdS host and Mn dopants continually changes during shell passivation. Prior to the shelling, the host-dopant coupling is strong as indicated by the single emission band (i.e., $I_{CdS}/I_{Mn} = 0$). After the growth of 5 shell MLs, the final CdS to Mn PL ratio (I_{CdS}/I_{Mn}) reached 2.08 and 3.40 for the Mn:CdS/ZnS$_{(1–5\ MLs)}$ and Mn:CdS/CdZnS$_{(1\ ML)}$/ ZnS$_{(1–4\ MLs)}$ QDs, respectively (Fig. 2c). The changes in the PL ratio of CdS QDs and Mn reflects different energy transfer rates between the excitons and Mn ions, which can be understood using eqn (1):[28]

$$\frac{I_{Mn}}{I_{QD}} = n\Phi_{Mn}\frac{k_{ET}}{k_{UD-R}}\frac{\lambda_{QD}}{\lambda_{Mn}} \quad (1)$$

where I_{Mn} and I_{QD} are intensities of Mn and host band-gap PL of the doped QDs, respectively; n is the number of Mn ions
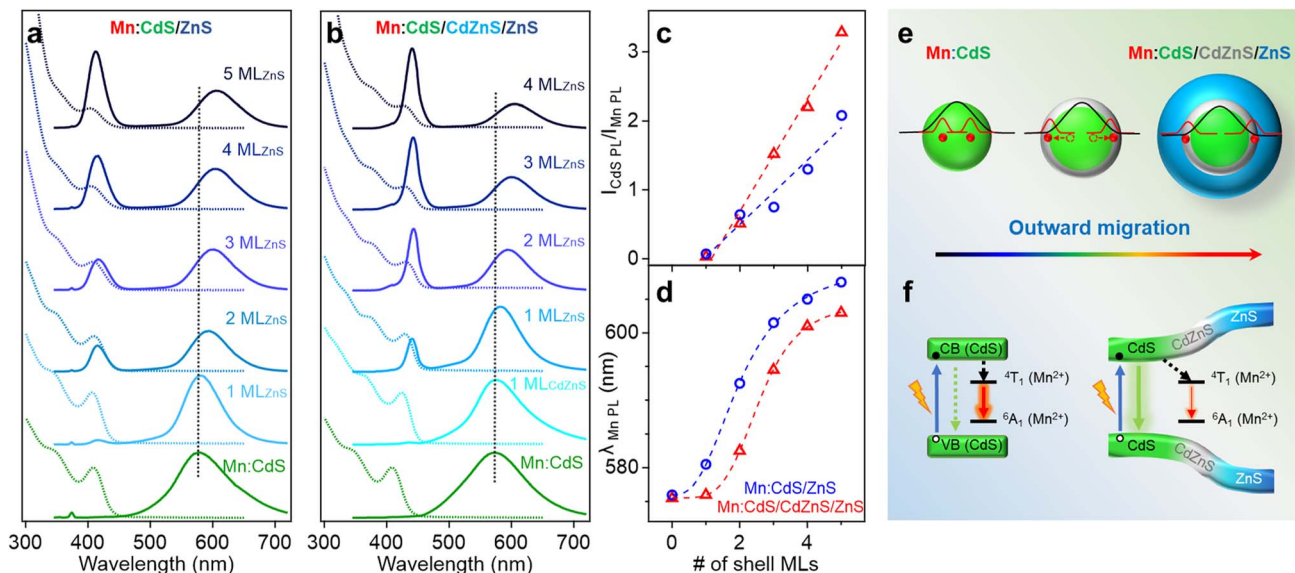
Fig. 2 (a and b) Normalized absorption (dotted lines) and PL (solid lines) spectra of Mn:CdS/ZnS$_{(1-5 MLs)}$ and Mn:CdS/CdZnS/ZnS$_{(1-4 MLs)}$ core/multi-shell QDs, respectively. (c) The PL Intensity ratio of CdS host lattice and Mn(II) and (d) the changes of Mn(II) PL peak position as a function of ZnS and CdZnS/ZnS shell thickness for Mn:CdS/ZnS$_{(1-5 MLs)}$ and Mn:CdS/CdZnS/ZnS$_{(1-4 MLs)}$ core/multi-shell QDs, respectively. (e) Schematic of the dopant outward migration by inserted CdZnS alloyed trap layer and (f) the band alignment of the Mn:CdS/CdZnS/ZnS core/multi-shell QDs.

doped inside one NC; λ_{QD} is the wavelength of the host QD PL, λ_{Mn} is the wavelength of the Mn emission; Φ_{Mn} is the emission efficiency of a Mn ion; k_{UD-R} is the radiative relaxation rate constant of undoped NCs; and k_{ET} is the rate constant for the energy transfer from an exciton to a Mn ion. Considering small changes in the host and dopant PL position, and constant doping concentrations in core/shell NCs, the k_{ET} between host QDs and Mn(II) dopants can be held proportional to the PL ratio amid the Mn and host lattice ($k_{ET} \propto I_{Mn}/I_{BG}$).[20,23,38] k_{ET} is related to the overlap between the wavefunctions of the exciton and Mn dopants,[38] and thus the distance between exciton and Mn ions. Therefore, the ratio of Mn(II) to host PL reflects the degree of host-to-dopant energy transfer rate and can be used as an "optical gauge" to monitor dopant location and dopant migration behavior inside core/shell QDs.[39] The dramatically increased PL ratio of CdS and Mn in Mn:CdS/CdZnS$_{(1 ML)}$/ZnS$_{(4 ML)}$ core/multi-shell QDs (from 0 to 3.40) indicates the decreased energy transfer efficiency (k_{ET}) and the host-dopant coupling due to the larger separation between the core and dopant ions during outward dopant ion migration (Fig. 2e and f).

The driving force of Mn(II) ions migration to the CdZnS shell is that the size of the Mn(II) ions (80 pm) is between that of Cd(II) (92 pm) and Zn(II) (74 pm).[40] Considering the nearly linear composition-dependent lattice parameter of the alloy phase based on Vegard's law,[33,41] the alloyed shell would then have intermediate lattice parameters with a cation size between that of Cd(II) and Zn(II). The Mn(II) migration from the CdS core to the alloyed shell is thermodynamically favored since it minimizes the lattice strain caused by the large size difference (13%) between Cd(II) and Mn(II) (Fig. S5†).[35] The moderately increased I_{CdS}/I_{Mn} (2.08) in the Mn:CdS/ZnS$_{(5 ML)}$ core/shell QDs without inserting the CdZnS alloyed layer could be understood by Mn

migration to a thin alloyed interface (Cd$_x$Zn$_{1-x}$S) formed by ion diffusion and exchange to release the strain caused by lattice mismatch (7% between CdS and ZnS), which is consistent with a small blueshift of the host PL. The elevated I_{CdS}/I_{Mn} ratio in Mn:CdS/CdZnS$_{(1 ML)}$/ZnS$_{(4 ML)}$ core/multi-shell QDs can be attributed to the greater distance travelled by the dopant ions in the presence of an inserted alloyed "trap" shell.

It should be noted that the nonradiative relaxation and surface defect emission could compete with the host-dopant energy transfer.[42] To verify that the change of the Mn-to-host PL ratio (as an "optical gauge" for dopant location) is due to dopant migration inside core/shell QDs instead of simple elimination of surface traps on the core QDs during shell coating, we performed a control experiment of undoped core/multi-shell QDs with the same core and shell composition and sizes. During the ZnS shell passivation, PL QYs for both the doped and undoped QDs increased from ∼5% to ∼30% with the increase of the shell thickness (Fig. S6†). The total PL QYs of Mn doped CdS/CdZnS/ZnS and CdS/ZnS QDs are similar to that of undoped QDs with the same shell thickness. Therefore, the changes in the ratio between host and Mn PL in the Mn:CdS/CdZnS/ZnS QDs can be explained by the different host-dopant energy transfer efficiency within the core/shell QDs due to the dopant migration towards alloyed layer, as the distance and wavefunction overlap between the core CdS and Mn dopant ions changes (Fig. 2e). Interestingly, it was found that the PL QYs of Mn doped core/shell QDs are slightly higher than their undoped counterparts regardless of the presence of the CdZnS alloyed trap layer. The slightly higher PL QY of Mn doped QDs compared with undoped ones is attributed to the fast host-dopant energy transfer that efficiently competes with nonradiative relaxation pathways, which is consistent with a previous report.[24]

The radial position of the Mn dopants inside the core/shell QDs can also be monitored by the Mn PL peak position because Mn PL is very sensitive to the shell applied pressure (proportional to shell thickness) based on the spherically symmetric elastic continuum model.[43] Dubertret et al. found that the additional pressure from the outside ZnS shell on the Mn dopants in Mn doped CdS/ZnS core/shell QDs slightly narrows the crystal field splitting of the Mn(II) d–d transition (from $^4T_1$ to $^6A_1$), causing a redshift in the Mn(II) PL.[43] The Mn PL of the Mn:CdS/ZnS core/shell QDs exhibit a rapid red-shift (∼30 nm) followed by gradual plateauing during the shelling process. However, no significant red-shift of Mn PL peak occurred after initial CdZnS alloyed shell passivation, and had a smaller total Mn PL red-shift of 28.5 nm for the ZnS shelled Mn:CdS/CdZnS$_{(1\ ML)}$/ZnS$_{(4\ ML)}$ core/multi-shell QDs (Fig. 2d). The decreased red-shift caused by the inserted CdZnS shell indicates a decrease in total shell-induced pressure on the dopants, which is consistent with "outward" dopant migration within the core/shell QDs.

Controlled inward dopant migration in Mn shell-doped core/multi-shell QDs

To expand the atomic trapping strategy for directional dopant migration, we then explored the inward Mn migration behavior by inserting CdZnS alloyed shell in Mn shell-doped core/multi-shell QDs. The Mn(II) dopant behaviors when doped into both smaller substitutional Zn sites and larger substitutional Cd sites in the shell lattice were tested.

Mn doping into ZnS shell with smaller initial substitutional Zn sites (74 pm)

We first synthesized undoped CdS core QDs, followed by inserting a CdZnS alloyed shell before the dopant growth in the ZnS shell (i.e., CdS/CdZnS$_{(1\ ML)}$/Mn:ZnS/ZnS$_{(1–3\ MLs)}$ core/multi-shell QDs) using a SILAR method. Successful shell growth was evidenced by the gradual size increase of QDs from 3.0 ± 0.3 nm of the CdS core QDs to 6.4 ± 0.3 nm after 1 ML CdZnS and 5 MLs ZnS shell coating from TEM images (Fig. 3a–c), as well as gradual XRD peak shift from cubic CdS to cubic ZnS phase with the increase of the ZnS shell thickness (Fig. 3d, and S7†).

Fig. 3e shows the absorption and PL spectra of CdS/CdZnS/Mn:ZnS/ZnS core/multi-shell QDs. The CdS core QDs exhibit an absorption peak around 404 nm and a broad defect emission peak centered around 580 nm. A new bandgap emission peak from CdS QDs at around 420 nm was observed after the growth of the first CdZnS shell. 1 ML ZnS shell on the surface of CdS/CdZnS/Mn:ZnS QDs leads to a Mn PL around 587 nm. As the ZnS shell MLs increase, the Mn PL peak redshifts indicating the shell thickness-dependent pressure applied on the Mn dopants (Fig. 3e, g and S8†). Surprisingly, no significant change in the PL ratio of Mn and CdS (I_{Mn}/I_{CdS}) of the core/multi-shell QDs with different ZnS shell thickness occurred (Fig. 3f), which indicates no significant dopant migration towards the inserted alloyed shell when Mn(II) dopants were directly doped into ZnS shell. Based on this result, we hypothesized that there might be a high energy barrier for dopant hopping when dopants occupy
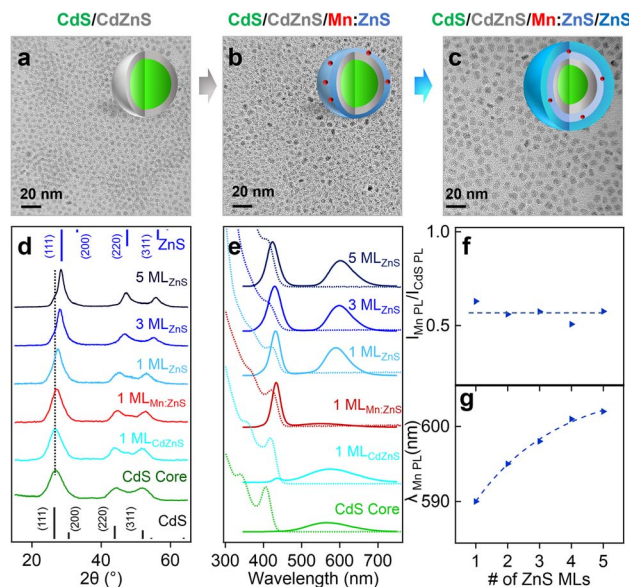

Fig. 3 (a–c) TEM images of CdS/CdZnS, CdS/CdZnS/Mn:ZnS, and CdS/CdZnS/Mn:ZnS/ZnS core/multi-shell QDs. (d) XRD patterns and (e) normalized absorption (dotted lines) and PL (solid lines) spectra of CdS core and CdS/CdZnS/Mn:ZnS/ZnS$_{(1–5\ MLs)}$ core/multi-shell QDs. (f) The PL Intensity ratio of Mn(II) and CdS host lattice ($I_{Mn\ PL}/I_{CdS\ PL}$) and (g) the Mn(II) PL peak position as a function of ZnS shell thickness.

a smaller Zn(II) substitutional site (74 pm) for a Mn(II) dopant (80 pm). In contrast, a larger initial substitutional site could lead to a lower energy barrier for dopant hopping, which allows for efficient atomic trapping and dopant migration.

Mn doping into larger substitutional Cd sites (92 pm) in shell

To study the initial substitutional site-dependent dopant behavior under the influence of the alloyed "trap" layer, Mn(II) ions were doped in CdS shell with larger substitutional Cd(II) cationic sites (92 nm) in CdS/CdZnS/Mn:CdS/ZnS core/multi-shell QDs. TEM images indicate the size of the core/multi-shell QDs increases ∼0.5 nm upon the addition of each shell layer (Fig. 4a–c), which is similar to that of CdS/CdZnS$_{(1\ ML)}$/Mn:ZnS/ZnS core/multi-shell QDs (Fig. S9†). XRD diffraction peaks gradually shifted from cubic CdS to cubic ZnS phase as the function of the ZnS shell thickness (Fig. 4d and S10†). ICP-OES measurements indicate that the Mn doping concentration is 0.4% for CdS/CdZnS/Mn:CdS QDs, which represents ∼5 Mn(II) ions per QD with an average diameter of a 3.8 nm. After the 1st ML of ZnS coating onto the QDs, the Mn doping concentration dropped to 0.3% which represents ∼4 Mn(II) ions per QD with an average diameter of 4.3 nm.

EPR data illustrates the hyperfine peaks with hyperfine splitting constants of 91.4 G and 68.5 G from surface and core Mn dopants for the CdS/CdZnS/Mn:CdS QDs, respectively (Fig. 4e). For the CdS/CdZnS/Mn:CdS/ZnS QDs core/multi-shell QDs, all surface hyperfine terms were removed through ZnS shell coating. Interestingly, the linewidth of the core Mn hyperfine splitting peaks of the CdS/CdZnS/Mn:CdS/ZnS$_{(1–5\ MLs)}$ QDs decreased from 8.6 G (1st ZnS ML) to 5.0 G (5th ZnS MLs) (Fig. 4f and g). Considering a slightly larger average Mn–Mn
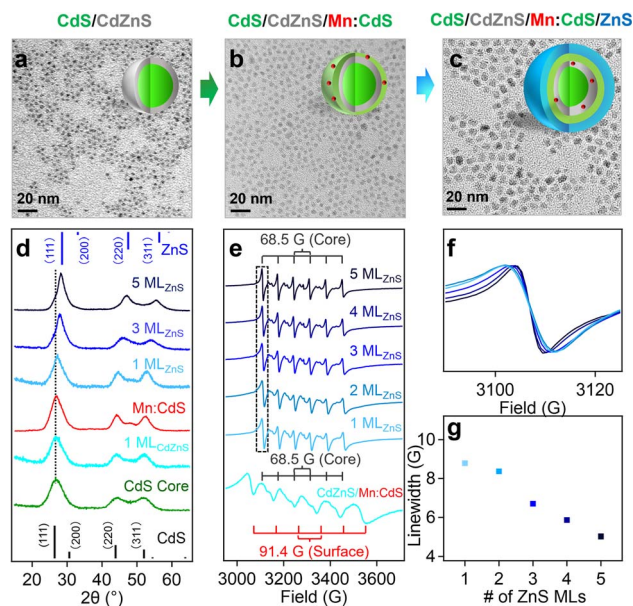
Fig. 4 (a–c) TEM images of CdS/CdZnS, CdS/CdZnS/Mn:CdS, and CdS/CdZnS/Mn:CdS/ZnS core/multi-shell QDs. (d) XRD patterns of CdS and CdS/CdZnS/Mn:CdS/ZnS core/multi-shell QDs. (e) X-band EPR spectra of CdS/CdZnS/Mn:CdS and CdS/CdZnS/Mn:CdS/ZnS$_{(1–5 \text{ MLs})}$ core/multi-shell QDs. (f) The representative first sextet hyperfine peak of EPR spectra to display general decreasing spectral linewidth and (g) the EPR hyperfine peak linewidth as a function of shell monolayers.

homogeneous Mn bonding environments, as the result of dopant migration towards the alloy trap layer with the smaller cationic size mismatch with Mn dopants.

To further prove the role of the alloyed trap layer for dopant migration, we used a CdS layer to replace CdZnS in the core/multi-shell QDs (*i.e.*, CdS/CdS/Mn:CdS/ZnS) without an "atomic trap" in the core/shell interface (Fig. S11 and S12†). Two similar sets of EPR hyperfine splitting from surface and core Mn dopants (A: 96.0 and 69.1 G) from CdS/CdS/Mn:CdS QDs and only core hyperfine peaks were observed after the following ZnS shell coating in CdS/CdS/Mn:CdS/ZnS QDs (Fig. S13†). However, no change in the linewidth of the Mn core hyperfine peaks (7.5 G for QDs from the 1st to 5th ZnS shell) was observed (Fig. S13b and c†), which indicates no significant changes in the dopant bonding environment and location inside the QD lattice without the CdZnS alloyed trap layer.

The absorption and PL spectra of the selected CdS/CdZnS/Mn:CdS/ZnS and CdS/CdS/Mn:CdS/ZnS core/multi-shell QDs are shown in Fig. 5a and b, respectively (full set optical data in Fig. S14†). The PL QYs of the QDs gradually increased during the ZnS shell passivation, which is similar to undoped core/multi-shell QDs with the same core and shell lattice (Fig. S15†). Significantly, the PL intensity ratio of Mn(II) and CdS host lattice ($I_{\text{Mn}}/I_{\text{CdS}}$) increases from 1.22 to 2.50 during the ZnS shell growth (1–5 MLs) in the CdS/CdZnS/Mn:CdS/ZnS core/multi-shell QDs (Fig. 5c), which is in contrast to the lack of a change in $I_{\text{Mn}}/I_{\text{CdS}}$ when doping Mn in the ZnS lattice of CdS/CdZnS/Mn:ZnS/ZnS core/multi-shell QDs. (Discussed in Mn doping into ZnS shell with smaller initial substitutional Zn sites above.)

Based on eqn (1), the increased PL ratio between Mn(II) and CdS host lattice represents increased rate of energy transfer (k_{ET}), which indicates the enhanced host-to-dopant energy
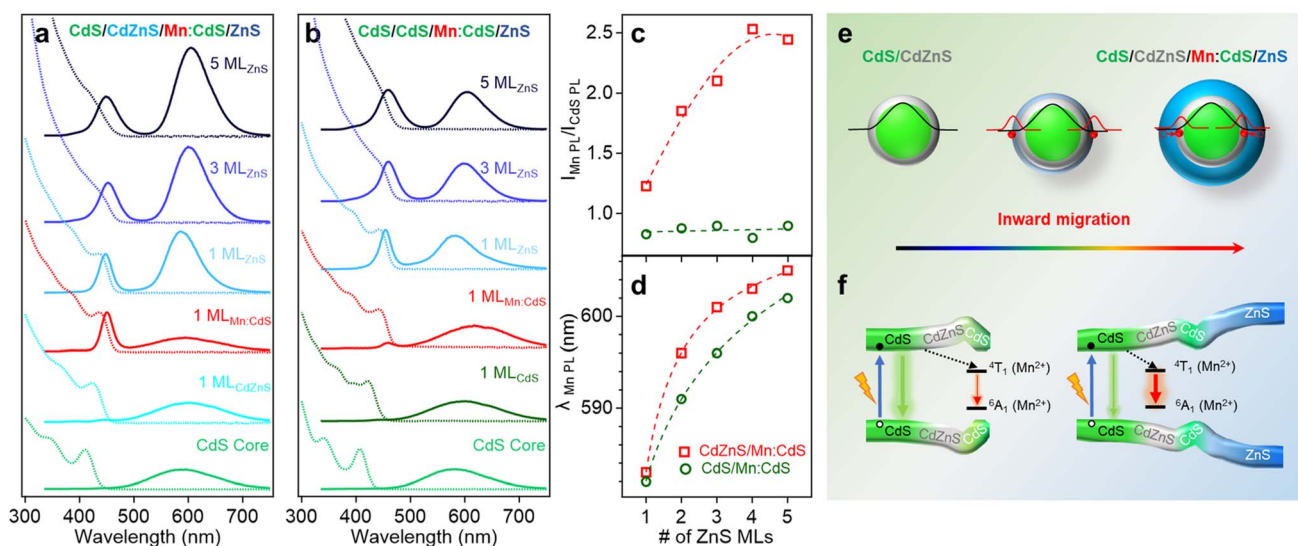
distance after the inward dopant migration in the core/multi-shell QDs (from ~1.7 nm to ~2.1 nm. See ESI† for the calculation, Table S3, and Scheme S1†), the decreasing hyperfine peak linewidth could indicate more diluted Mn doping inside the inserted alloy trap layer, as well as narrower and more

Fig. 5 (a and b) Normalized absorption and PL spectra of (a) CdS/CdZnS/Mn:CdS/ZnS$_{(1–5 \text{ MLs})}$ and (b) CdS/CdS/Mn:CdS/ZnS$_{(1–5 \text{ MLs})}$ core/multi-shell QDs. (c) The PL Intensity ratio of Mn(II) and CdS host lattice and (d) the changes of Mn(II) PL peak position as a function of ZnS shell thickness. (e) Schematic of the dopant inward migration by inserted CdZnS alloyed trap layer and (f) the band alignment of the CdS/CdZnS/Mn:CdS/ZnS core/multi-shell QDs.

transfer due to the inward Mn migration to the alloyed interface (Fig. 5e and f). Furthermore, there was no significant change in the PL ratio of Mn(II) and CdS host QDs when a CdS layer is used to replace the "atomic trap" CdZnS layer in the CdS/CdS/Mn:CdS/ZnS core/multi-shell QDs (Fig. 5b and c), which indicates there was no significant dopant migration in the absence of the alloyed interface even though Mn dopants substitute in larger Cd sites. In addition, a rapid redshift of the Mn PL position (23 nm) was observed in the CdS/CdZnS/Mn:CdS/ZnS QDs with the inserted alloy trap (Fig. 5a and d). In contrast, the Mn dopant PL peak position of CdS/CdS/Mn:CdS/ZnS QDs experienced a lesser redshift (20 nm, Fig. 5b and d). The larger Mn PL peak shift indicates larger pressure applied from the thick outer shell in CdS/CdZnS/Mn:CdS/ZnS QDs, which can support that the alloy trap layer could facilitate the inward dopant migration (Fig. 5e).

Mechanism of initial dopant site-dependent dopant migration behavior and DFT calculations

Our experimental results indicate significant dopant migration when Mn(II) ions were doped at larger Cd(II) substitutional cationic sites (92 pm) in Mn:CdS/CdZnS/ZnS (outward migration) and CdS/CdZnS/Mn:CdS/ZnS core/multi-shell QDs (inward migration) under the influence of inserted CdZnS "atomic trap". The large size mismatch (13%) between a Mn(II) dopant and a larger Cd(II) substitutional site (Mn_{Cd}^X) entails significant local distortion of the structure, therefore, thermodynamically, the dopant migration to the alloyed shell with smaller size mismatch ($Mn_{Cd/Zn}^X$) to reduce the cationic size strain between Mn(II) ions and host sites is favored. However, no significant dopant migration towards inserted alloyed shell occurred when Mn(II) dopants were directly doped into ZnS shell with smaller Zn(II) cationic sites (74 pm) as in CdS/CdZnS/Mn:ZnS/ZnS core/multi-shell QDs. Therefore, the initial doping environment can

affect the dopant behavior, which can be understood as the different energy barriers for the Mn dopants hopping between the T_d sites formed in the cubic close packing of S ions. In general, the dopant ions will follow the lowest energy path available in the host lattice during migration, in which the dopant ion first passes through one of the triangular faces of the T_d site, then through one of the triangular faces of an adjacent tetrahedron, before arriving at the vacant tetrahedral site ($V_{Cd/Zn}^{''}$, Fig. 6a and b).

In the case of Mn doped at a smaller Zn(II) substitutional site (74 pm, Mn_{Zn}^X), a high activation energy for dopant hopping is expected since the dopant needs to move through a small triangular face from the host ZnS_4 tetrahedron (Fig. 6b). The high activation energy for dopants escaping from the small tetrahedrons leads to inactive dopant trapping of the alloyed T_d site. Therefore, no notable dopant migration occurs in our experiments even though with the inserted "alloyed trap" layer. In contrast, a larger initial substitutional Cd(II) site (92 pm) in CdS lattice with larger triangular faces of the host CdS_4 tetrahedron could lead to a lower energy barrier for dopant hopping (Fig. 6a), which allows for active/efficient atomic trapping and directional dopant migration towards alloyed lattice under moderate temperatures ($Mn_{Cd}^X + V_{Cd/Zn}^{''} \rightarrow Mn_{Cd/Zn}^X + V_{Cd}^{''}$).

To further confirm the initial doping site-dependent dopant behaviors, the minimum energy path (MEP) of the Mn dopant hopping to escape from the T_d site in ZnS and CdS lattice was calculated using DFT. The transition-state structure for the Mn migration was obtained by constraining the Mn to be co-planar with one of the triangular faces of the T_d site (Fig. 6a and b). The direction normal to the plane, defined by the three S and the Mn atoms, was identified to the unbound reaction coordinate which was used to construct the MEP for Mn migration (Fig. 6c). The zero of the hopping distance (x-axis in Fig. 6c) corresponds to the minimum-energy structure of the Mn in the T_d site. The barrier height (E^a) is defined as the energy difference between the transition-state and the minimum-energy structure for both CdS and ZnS T_d sites. The results from the MEP analysis show that the E^a is 0.71 and 0.47 eV at 0 K for ZnS_4 and CdS_4 T_d sites, respectively, which represents a 52% higher energy barrier for the Mn hopping in the ZnS lattice as compared to the CdS lattice.

The barrier height (E^a) was further used to calculate the temperature-dependence relative rate constant of dopant migration using transition-state theory[44] (Fig. 6d). The relative temperature dependence of the mobility of the ions can be expressed by an Arrhenius-like equation.

$$\frac{k_{ZnS}}{k_{CdS}} = \frac{\exp\left[-E_{ZnS}^a/k_B T\right]}{\exp\left[-E_{CdS}^a/k_B T\right]} \quad (2)$$

Analysis of the relative rate constants show that the rate of Mn dopant migration is about three-orders of magnitude smaller (0.0018–0.004) in the ZnS lattice as compared to CdS for the temperature range investigated in this study (180–230 °C, blue region in Fig. 6d). It should be noted that higher thermal energy of dopant ions at elevated temperatures (>230 °C) could
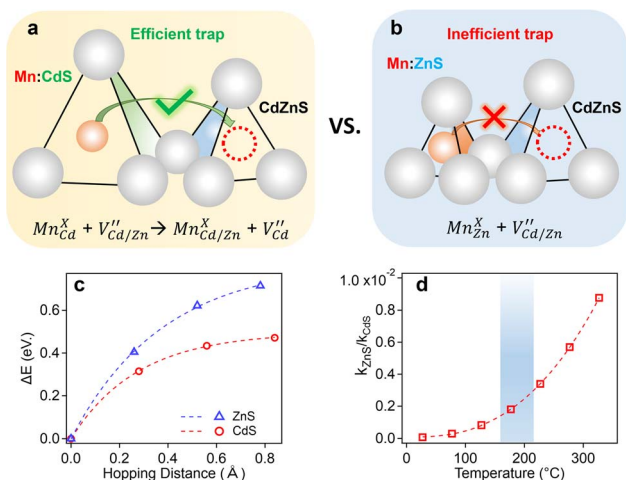

Fig. 6 Schematic of dopant migration behaviors when a Mn dopant occupies a larger substitutional Cd site in QD lattice (a) and a smaller substitutional Zn site in QD lattice (b). (c) DFT calculation of the minimum energy path as a function of the reaction coordinate (Z) at 0 K. (d) Ratio of rate constant for dopant migration in ZnS and CdS lattices as a function of temperature.

lead to fast dopant migration due to the increased hopping frequencies of the dopants inside the host lattice.[26] However, the rate of Mn dopant migration in the ZnS lattice as compared to CdS is still more than two-orders of magnitude smaller (0.005–0.01) at 230–320 °C shown in Fig. 6d, which can support the different dopant behaviors when dopants initially substitute in Cd and Zn sites in the core/multi-shell QDs.

Conclusions

In this work, directional dopant migration behaviors including outward and inward migration were achieved using an alloyed layer with a small cationic size mismatch with the dopant ions in Mn core-doped and shell-doped core/multi-shell QDs, respectively. The inserted alloyed shell (CdZnS) with smaller cationic size mismatch with the dopants can serve as an "atomic trap" to the dopant ions to reduce the strain from the larger cationic mismatch between Mn(II) ions and host sites. In addition, the initial dopant substantial site is critical for the dopant migration behavior. Specifically, larger Cd(II) substitutional sites for Mn dopants in the core (shell)-doped core/multi-shell QDs with inserted CdZnS "active atomic trap" facilitate either the outward or inward dopant migration, while smaller initial substitutional sites inhibit dopant movement due to higher energy barrier for dopant hopping even through more stable alloyed substitutional sites are available (*i.e.*, "inefficient atomic trap"). This work represents the first directional dopant migration behavior in NC lattice by inserting an "atomic trap" for dopant ions. Controlled dopant migration inside NC lattice provides a new way to fine tune the properties of doped QDs.

Data availability

The additional ESI,† including experimental details and all characterization data (XRD, TEM, optical spectra and EPR) are available in the ESI.†

Author contributions

W. Z. directed the project. C. C. and W. Z. conceived and designed the project. C. C. and E. H. performed all the experiments. C. G. and A. C. performed DFT calculations. S. L., H. L., and W. M. assisted in TEM and XRD experiments. J. M. F. and R. W. M. assisted in EPR measurements and analysis. C. C. and W. Z. co-wrote the manuscript. All authors discussed the results and commented on the manuscript.

Conflicts of interest

There are no conflicts to declare.

Acknowledgements

Notes and references

1 D. J. Norris, A. L. Efros and S. C. Erwin, Doped nanocrystals, *Science*, 2008, **319**, 1776–1779.

2 Y. C. Cao, Materials science. Impurities enhance semiconductor nanocrystal performance, *Science*, 2011, **332**, 48–49.

3 R. E. Bailey and S. Nie, Alloyed semiconductor quantum dots: tuning the optical properties without changing the particle size, *J. Am. Chem. Soc.*, 2003, **125**, 7100–7106.

4 S. C. Erwin, L. Zu, M. I. Haftel, A. L. Efros, T. A. Kennedy and D. J. Norris, Doping semiconductor nanocrystals, *Nature*, 2005, **436**, 91–94.

5 D. Mocatta, G. Cohen, J. Schattner, O. Millo, E. Rabani and U. Banin, Heavily doped semiconductor nanocrystal quantum dots, *Science*, 2011, **332**, 77–81.

6 T. Zuo, Z. Sun, Y. Zhao, X. Jiang and X. Gao, The big red shift of photoluminescence of Mn dopants in strained CdS: a case study of Mn-doped MnS-CdS heteronanostructures, *J. Am. Chem. Soc.*, 2010, **132**, 6618–6619.

7 S. Das Adhikari, S. K. Dutta, A. Dutta, A. K. Guria and N. Pradhan, Chemically tailoring the dopant emission in manganese-Doped $CsPbCl_3$ perovskite nanocrystals, *Angew. Chem., Int. Ed.*, 2017, **56**, 8746–8750.

8 J. C. Bear, N. Hollingsworth, P. D. McNaughter, A. G. Mayes, M. B. Ward, T. Nann, G. Hogarth and I. P. Parkin, Copper-doped CdSe/ZnS quantum dots: controllable photoactivated copper(I) cation storage and release vectors for catalysis, *Angew. Chem., Int. Ed.*, 2014, **53**, 1598–1601.

9 R. Beaulac, L. Schneider, P. I. Archer, G. Bacher and D. R. Gamelin, Light-induced spontaneous magnetization in doped colloidal quantum dots, *Science*, 2009, **325**, 973–976.

10 K. E. Knowles, K. H. Hartstein, T. B. Kilburn, A. Marchioro, H. D. Nelson, P. J. Whitham and D. R. Gamelin, Luminescent colloidal semiconductor nanocrystals containing copper: synthesis, photophysics, and applications, *Chem. Rev.*, 2016, **116**, 10820–10851.

11 R. Buonsanti and D. J. Milliron, Chemistry of doped colloidal nanocrystals, *Chem. Mater.*, 2013, **25**, 1305–1317.

12 N. Pradhan, S. Das Adhikari, A. Nag and D. D. Sarma, Luminescence, plasmonic, and magnetic properties of doped semiconductor nanocrystals, *Angew. Chem., Int. Ed.*, 2017, **56**, 7038–7054.

13 W. Zheng, P. Kumar, A. Washington, Z. Wang, N. S. Dalal, G. F. Strouse and K. Singh, Quantum phase transition from superparamagnetic to quantum superparamagnetic state in ultrasmall $Cd_{(1-x)}Cr(II)_{(x)}Se$ quantum dots?, *J. Am. Chem. Soc.*, 2012, **134**, 2172–2179.

14 K. R. Kittilstved and D. R. Gamelin, Activation of high-$T_{(C)}$ ferromagnetism in Mn^{2+}-doped ZnO using amines, *J. Am. Chem. Soc.*, 2005, **127**, 5292–5293.

15 C. Pu, J. Ma, H. Qin, M. Yan, T. Fu, Y. Niu, X. Yang, Y. Huang, F. Zhao and X. Peng, Doped semiconductor-nanocrystal emitters with optimal photoluminescence decay dynamics in microsecond to millisecond range: synthesis and applications, *ACS Cent. Sci.*, 2016, **2**, 32–39.

16 J. H. Yu, X. Liu, K. E. Kweon, J. Joo, J. Park, K. T. Ko, D. W. Lee, S. Shen, K. Tivakornsasithorn, J. S. Son, J. H. Park, Y. W. Kim, G. S. Hwang, M. Dobrowolska, J. K. Furdyna and T. Hyeon, Giant Zeeman splitting in nucleation-controlled doped CdSe:Mn^{2+} quantum nanoribbons, *Nat. Mater.*, 2010, **9**, 47–53.

17 E. Hofman, A. Khammang, J. T. Wright, Z. J. Li, P. F. McLaughlin, A. H. Davis, J. M. Franck, A. Chakraborty, R. W. Meulenberg and W. Zheng, Decoupling and coupling of the host-dopant interaction by manipulating dopant movement in core/shell quantum dots, *J. Phys. Chem. Lett.*, 2020, **11**, 5992–5999.

18 R. Beaulac, S. Ochsenbein and D. Gamelin, *Colloidal transition-metal-doped quantum dots*, CRC Press, 2nd edn, 2010.

19 R. Beaulac, P. I. Archer and D. R. Gamelin, Luminescence in colloidal Mn^{2+}-doped semiconductor nanocrystals, *J. Solid State Chem.*, 2008, **181**, 1582–1589.

20 J. D. Bryan and D. R. Gamelin, Doped semiconductor nanocrystals: synthesis, characterization, physical properties, and applications, *Prog. Inorg. Chem.*, 2005, **54**, 47–126.

21 Y. Yang, O. Chen, A. Angerhofer and Y. C. Cao, On doping CdS/ZnS core/shell nanocrystals with Mn, *J. Am. Chem. Soc.*, 2008, **130**, 15649–15661.

22 Y. Yang, O. Chen, A. Angerhofer and Y. C. Cao, Radial-position-controlled doping in CdS/ZnS core/shell nanocrystals, *J. Am. Chem. Soc.*, 2006, **128**, 12428–12429.

23 Y. Yang, O. Chen, A. Angerhofer and Y. C. Cao, Radial-position-controlled doping of CdS/ZnS core/shell nanocrystals: surface effects and position-dependent properties, *Chem.–Eur. J.*, 2009, **15**, 3186–3197.

24 H. Y. Chen, S. Maiti and D. H. Son, Doping location-dependent energy transfer dynamics in Mn-doped CdS/ZnS nanocrystals, *ACS Nano*, 2012, **6**, 583–591.

25 R. Beaulac, P. I. Archer, S. T. Ochsenbein and D. R. Gamelin, Mn^{2+}-doped CdSe quantum dots: new inorganic materials for spin-electronics and spin-photonics, *Adv. Funct. Mater.*, 2008, **18**, 3873–3891.

26 L. Smart and E. E. A. Moore, *Solid State Chemistry: An Introduction*, CRC Press, 2012.

27 G. M. Dalpian and J. R. Chelikowsky, Self-purification in semiconductor nanocrystals, *Phys. Rev. Lett.*, 2006, **96**, 226802.

28 L. Zu, D. J. Norris, T. A. Kennedy, S. C. Erwin and A. L. Efros, Impact of ripening on manganese-doped ZnSe nanocrystals, *Nano Lett.*, 2006, **6**, 334–340.

29 H. Zhao, Y. Zhu, H. Ye, Y. He, H. Li, Y. Sun, F. Yang and R. Wang, Atomic-Scale structure dynamics of nanocrystals revealed by in situ and environmental transmission electron microscopy, *Adv. Mater.*, 2023, 2206911.

30 Z.-J. Li, E. Hofman, A. Blaker, A. Davis, B. Dzikovski, D.-K. Ma and W. Zheng, Interface engineering of Mn doped ZnSe-based core/shell nanowires for tunable host-dopant coupling, *ACS Nano*, 2017, **11**, 12591–12600.

31 Y. Cheng, Y. Xie, Z. Liu, S. Yan, Y. Ma, Y. Yue, J. Wang, Y. Gao and L. Li, Maximizing electron channels enabled by MXene aerogel for high-performance self-healable flexible electronic skin, *ACS Nano*, 2023, **17**, 1393–1402.

32 J. J. Li, Y. A. Wang, W. Guo, J. C. Keay, T. D. Mishima, M. B. Johnson and X. Peng, Large-scale synthesis of nearly monodisperse CdSe/CdS core/shell nanocrystals using air-stable reagents via successive ion layer adsorption and reaction, *J. Am. Chem. Soc.*, 2003, **125**, 12567–12575.

33 A. R. Denton and N. W. Ashcroft, Vegard's law, *Phys. Rev. A*, 1991, **43**, 3161–3164.

34 W. Zheng, Z. Wang, J. van Tol, N. S. Dalal and G. F. Strouse, Alloy formation at the tetrapod core/arm interface, *Nano Lett.*, 2012, **12**, 3132–3137.

35 A. Nag, S. Chakraborty and D. D. Sarma, To dope Mn^{2+} in a semiconducting nanocrystal, *J. Am. Chem. Soc.*, 2008, **130**, 10605–10611.

36 W. Zheng, Z. Wang, J. Wright, B. Goundie, N. S. Dalal, R. W. Meulenberg and G. F. Strouse, Probing the local site environments in Mn:CdSe quantum dots, *J. Phys. Chem. C*, 2011, **115**, 23305–23314.

37 P. Reiss, M. Protiere and L. Li, Core/Shell semiconductor nanocrystals, *Small*, 2009, **5**, 154–168.

38 S. T. O. Rémi Beaulac and D. R. Gamelin, *Colloidal Transition Metal-Doped Quantum Dots*, CRC Press, 2010.

39 E. Hofman, R. J. Robinson, Z. J. Li, B. Dzikovski and W. Zheng, Controlled dopant migration in CdS/ZnS core/shell quantum dots, *J. Am. Chem. Soc.*, 2017, **139**, 8878–8885.

40 R. D. Shannon, Revised effective ionic radii and systematic studies of interatomic distances in halides and chalcogenides, *Acta Crystallogr.*, 1976, **32**, 751–767.

41 B. O. Dabbousi, J. Rodriguez-Viejo, F. V. Mikulec, J. R. Heine, H. Mattoussi, R. Ober, K. F. Jensen and M. G. Bawendi, (CdSe)ZnS core–shell quantum dots: synthesis and characterization of a size series of highly luminescent nanocrystallites, *J. Phys. Chem. B*, 1997, **101**, 9463–9475.

42 J. H. Chung, C. S. Ah and D.-J. Jang, Formation and distinctive decay times of surface- and lattice-bound Mn^{2+} impurity luminescence in ZnS nanoparticles, *J. Phys. Chem. B*, 2001, **105**, 4128–4132.

43 S. Ithurria, P. Guyot-Sionnest, B. Mahler and B. Dubertret, Mn^{2+} as a radial pressure gauge in colloidal core/shell nanocrystals, *Phys. Rev. Lett.*, 2007, **99**, 265501.

44 T. Fueno, *Transition State: A Theoretical Approach*, CRC Press, Netherlands, 2019.